**The Thesis Committee for Kidam Mun**
**Certifies that this is the approved version of the following thesis:**

# STUDY OF THE APPLIED CURRENT ASYMMETRY OF THE SPIN-TORQUE INTERACTION

**APPROVED BY**
**SUPERVISING COMMITTEE:**

**Supervisor:**

James L. Erskine

Zhen Yao

# STUDY OF THE APPLIED CURRENT ASYMMETRY OF THE SPIN-TORQUE INTERACTION

**by**

**Kidam Mun**

**Thesis**

Presented to the Faculty of the Graduate School of

The University of Texas at Austin

in Partial Fulfillment

of the Requirements

for the Degree of

**Master of Arts**

**The University of Texas at Austin**

**August 2017**

# Dedication

This work is dedicated to my parents for all their love and care.

# Acknowledgements

I want to express my thanks especially to Prof. Dr. James L. Erskine, for the opportunity to work in his group, who also made the rough project outline, and who provided priceless advice in numerous discussions.

# Abstract

## STUDY OF THE APPLIED CURRENT ASYMMETRY OF THE SPIN-TORQUE INTERACTION

Kidam Mun, M.A.

The University of Texas at Austin, 2017

Supervisor: James L. Erskine

This thesis describes experimental work that is designed to address unresolved issues in domain-wall dynamics that have emerged from recent scientific work on magnetic field and electric-current driven domain-wall dynamics in permalloy microstructures. A principle issue involves nonlinear effects in the electric-current driven domain-wall velocity under reversal of electric current. Existing theoretical models of the spin-torque effect (responsible for electric-current driven domain-wall motion) do not allow nonlinear current response. Other issues are related to magnetic-field and electric-current driven Barkhausen jumps in magnetic microstructure. Sample preparation and characterization studies reported provide the technical basis for improved experiments that should resolve the stated unsettled scientific issues.

# Table of Contents

# List of Figures

# Chapter 1: Introduction and Description of Scientific Issues

A magnetic domain wall is the thin region between magnetic domains- a region of uniform electron spin alignment in a magnetic material. Manipulation of domain-walls provides a basis for a broad range of magnetic materials-based technologies that include magnetic sensors, data storage applications, lab-on-a-chip techniques for manipulating magnetic nanoparticles involving biomedical applications, and other electron spin-based magneto-electronic applications.

The ability to manipulate domain-walls at high speeds on nanometer scales by electric current (through the spin-transfer torque mechanism) has recently stimulated significant efforts to characterize and fully understand this important effect. Recent experiments that explore magnetic-field and electric-current driven domain-wall dynamics have verified the essential features of magnetic-field driven mobility models (domain-wall velocity as a function of applied magnetic field) that have been known for decades, and have explored the additional effects of including electric current in the mobility measurements.

An important discovery of these experiments is the observation of a nonlinear effect[1, 2] on domain-wall motion associated with electric current that is not explained by existing models of the spin-transfer torque effect. A primary motivation for work presented in this thesis is to prepare and characterize new nanometer-scale samples to explore and explain the nonlinear effect.

Figures 1.1 and 1.2 define and illustrate the nonlinear current effect[1] on domain-wall mobility and outline the sample requirements and measurement technique[3] used to observe the effect.

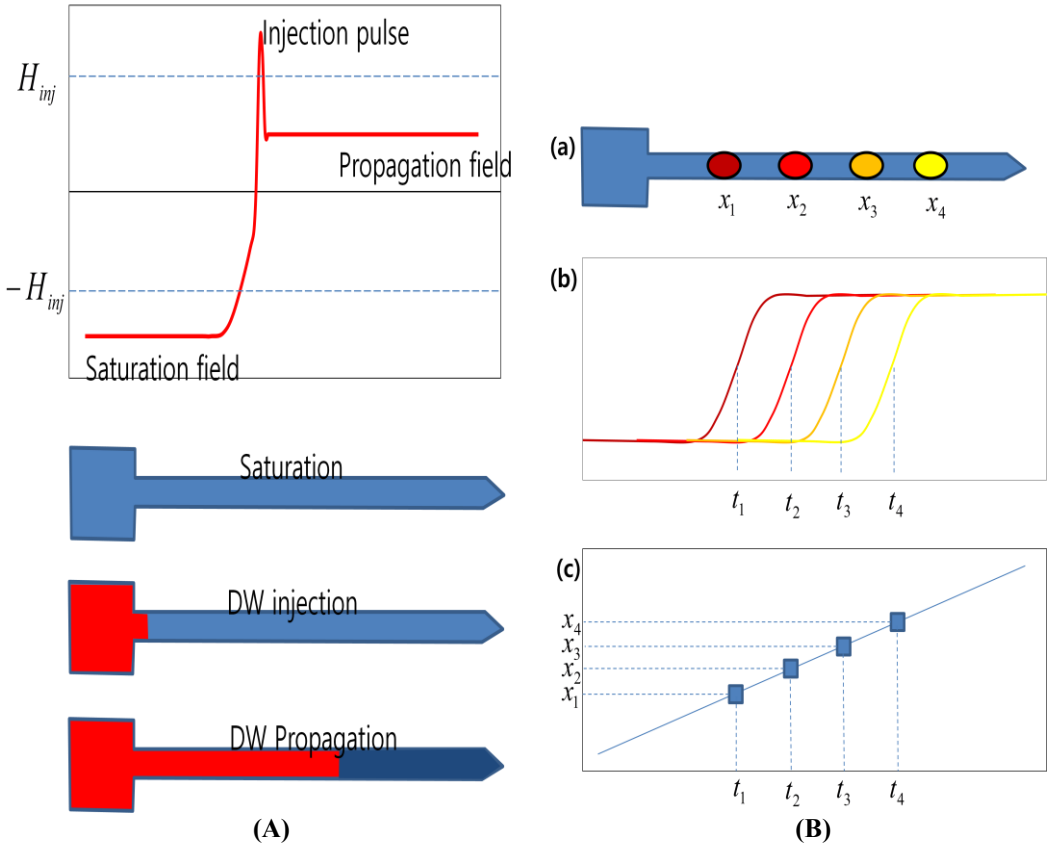


**Figure 1.1 Domain Wall injection and TOF Measurement**

Domain wall velocity was determined by a time-of-flight method. A uniformly magnetized nanowire is prepared by a saturation field. A high field injection pulse is used to overcome the potential well between injection pad and nanowire. The domain wall injected by field is propelled by a propagation field (applied field). TOF is determined by MOKE, the signal at $\chi_1, \chi_2, \chi_3, \chi_4$ position. Then, domain-wall velocity and mobility curves can be calculated from the TOF data.

Figure 1.1 illustrates the time-of-flight technique used to measure the magnetic-field driven domain-wall mobility[3] (velocity as a function of applied magnetic field). The magnetic structure consists of a 20nm thick rectangular cross-section permalloy nanowire and domain-wall injection pad [panel (a)]. A time-dependent magnetic field saturates the structure magnetization prior to domain-wall injection, followed by a fast injection pulse, and then a constant propagation field that establishes uniform domain-wall velocity. The magneto-optical Kerr effect (MOKE) is used to measure domain-wall time-of-flight from the injection pad to various locations $x_1, x_2, x_3, x_4$ along the

nanowire where the polarimeter beam is focused. A slight modification of the sample geometry permits application of electric current to the nanowire while conducting time-of-flight domain-wall mobility measurements.[1] This allows analysis of the effect of electric current (spin-transfer torque effects) on the field-driven mobility. The nanowire sample (inset of Fig 1.2) and mobility curves and displayed in Figure 1.2. This figure illustrates the unexplained nonlinear response to electric current. The domain-wall velocity is enhanced by current, but this enhancement is nonlinear with respect to sign of current resulting in non-symmetric shifts of the mobility curves.

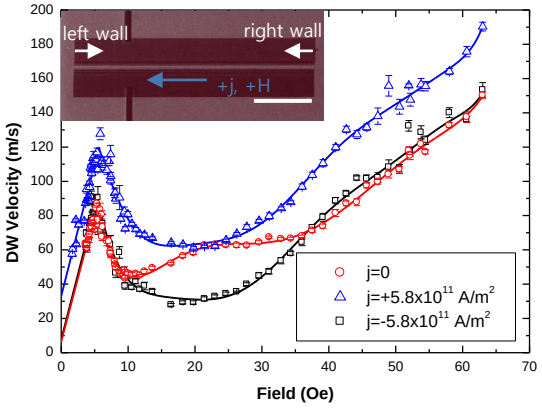


**Figure 1.2 Magnetic field and electric current driven mobility curves for left wall**
Constant electric current $+j$ is expected to increase the velocity of the left DW and decrease the velocity of the right DW because of the spin-torque force. However, experimental result shows $+j$ (electron flows in direction of DW velocity) increases the velocity, but $-j$ doesn't decrease the DW velocity as expected. Both positive and negative direction currents destroy the broad structure that appears in the $j=0$ mobility curve between 10 and 40 Oe. The structure in $v(H)$ at $j=0$ is associated with a stable vortex-antivortex DW structure, that propagates normally over a narrow drive-field range.

Existing theoretical models of spin-transfer torque effects predict linear in J-dependent shifts in domain-wall velocity, which is clearly not consistent with the experimental results of Fig.1.2. Resolving this issue is the primary motivation for the sample preparation and characterization studies presented in this thesis.

# Chapter 2: Basic Concepts in Micromagnetics

This chapter provides a brief review of basic concepts in ferromagnetism, domain formation and domain-wall structure, including models, both analytical and numerical simulation methods, that are required to describe and analyze domain-wall phenomena presented in this thesis.

## 2.1 Ferromagnetism

Spins of some metallic materials and alloys are ordered spontaneously, and this characteristic is called ferromagnetism. Exchange interaction (which is interaction between nearby electron spins) is the origin of this ordering. Heisenberg[5] introduced the Hamiltonian model which represents exchange interaction between nearby electron spins,

$$H = -\sum_{i,j} J_{i,j} \mathbf{S}_i \cdot \mathbf{S}_j, \qquad (2.1)$$

where the sum goes on the distinct pairs of spins, $\mathbf{S}_i$ and $\mathbf{S}_j$ at sites $i$ and $j$. $J_{i,j}$ is the exchange constant which represents the coupling between pairs of electron spins. In positive exchange constants case, parallel spin couples lower the energy. Thus, all the spins will be parallel to each other at the ground state, that is ferromagnetic. (Negative $J$ corresponds to anti-ferromagnetic.) This ordering is vanished by thermal agitation above certain temperature which is called Curie temperature.[6]

## 2.2 Energy in ferromagnetic material

### 2.2.1 Exchange Energy

Exchange interaction is the source of ferromagnetic energy which aligns the spin direction. The energy density of the exchange energy is known as :

$$E_{ex} = \frac{A}{\mathbf{M}^2} |\nabla \mathbf{M}|^2, \tag{2.2}$$

where $A$ is the exchange constant (material dependent), $\mathbf{M}$ is the magnetization which is the volume density of the net magnetic moment. $A$ is generally tensor, but it can be reduced to scalar for the isotropic material. Usually practical system is isotropic, and scalar $A$ is used.

### 2.2.2 Zeeman Energy

Interaction between external field and spin generates Zeeman effects. This energy density is

$$E_{Zeeman} = \mu_0 \mathbf{H}_{ex} \cdot \mathbf{M}, \tag{2.3}$$

where $\mu_0$ is vacuum susceptibility, $\mathbf{M}$ is magnetization, $\mathbf{H}_{ex}$ is external field. $E_{Zeeman}$ is minimized when the external field is parallel to magnetization direction.

### 2.2.3 Anisotropy Energy

Magnetization of material prefers certain direction in crystal. This preference is caused by anisotropy energy which originates from spin-orbit coupling. The electron's orbital motion is affected by lattice direction of crystals, and spin-orbit coupling is affected by lattice. As a result, spin direction favors certain directions by the lattice. This anisotropy energy density is

$$E_{an} = Kf(\alpha_1, \alpha_2, \alpha_3), \tag{2.4}$$

where $K$ is material dependent anisotropy constant ($J/m^3$), and $\alpha_1, \alpha_2, \alpha_3$ represent direction cosines of magnetization, $f$ is the function which includes the information of lattice. Magnetization direction that maximizes the anisotropy energy is hard axis, and that minimizes the anisotropy energy is easy axis.

### 2.2.4 Demagnetization Energy

The demagnetization field is generated by the sample magnetization itself, it is called stray field over the sample boundary. Each magnetic dipole in ferromagnetic material is affected by magnetic field of all other dipoles. Shape anisotropy is caused by this field. The energy density of the demagnetization field, $\mathbf{H}_{dm}$, is given by

$$E_{dm} = -\frac{1}{2}\mathbf{H}_{dm} \cdot \mathbf{M}. \qquad (2.5)$$

This energy is the main source of domain-wall creation .

## 2.4 Qualitative explanation of domain-wall

The formation of a magnetic domain wall in a ferromagnetic materials is a result of energy minimization. Exchange interaction, anisotropy, demagnetizing field, and external field are associated components of the energy. In thin films, domain-wall creation minimizes the stray fields.

At very short distance, exchange energy is the dominant factor, and a single-domain sample has a large stray field which stores high energy[Fig. 2.1(a)]. This field energy can be reduced when the domain splits into two domains with the magnetization in opposite direction in each region [Fig. 2.1.(b)]. The field energy can be also reduced by creation of closed domains where domain magnetization is perpendicular to others [Fig. 2.1(c)]. Then, entirely closed loop of flux is formed in the material, and in this case the stray field energy is minimized.

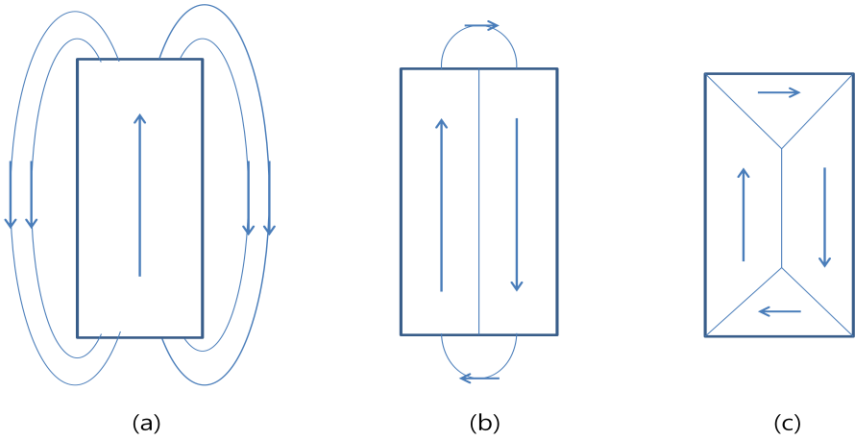


**Figure 2.1** Stray Field Energy is minimized by producing the additional Domains.

Direct evidence of the domain structure is the photomicrographs of domain boundaries obtained by the technique of magnetic powder pattern (F. Bitter) and MOKE signal.[7] There are two types of wall on magnetic structures, Bloch and Néel walls. In the Bloch wall case, the magnetization rotates in the plane perpendicular to the film surface. In thin-film structures, there is big demagnetization energy. The magnetization rotates in the film plane in the Néel wall type.

In the 1-D magnetic nanowire structures, there are two fundamental domain-wall types, transverse wall (TW) and vortex wall (VW). For a small cross-sectional nanowire structure, TW is a preferred domain wall structure (VW type for a large cross-sectional nanowire structures).

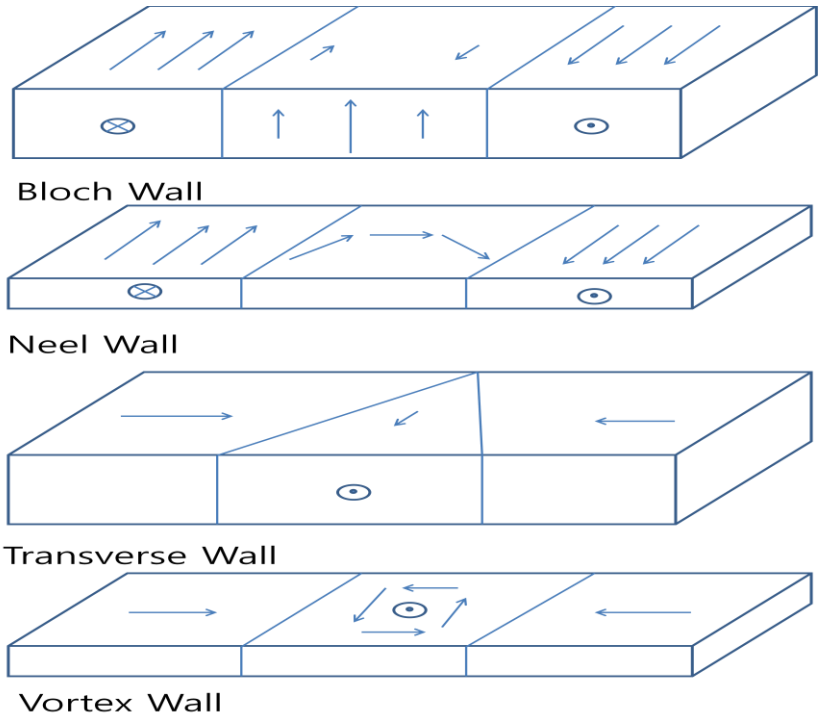


**Figure 2.2** Major Domain Wall Types: Bloch, Neel, Transverse, and Vortex Wall.

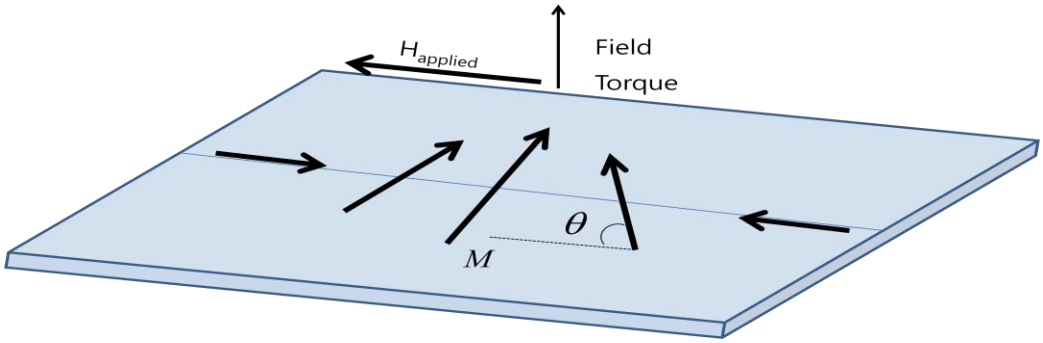


**(A) Initial spin confined on the 1-D state**

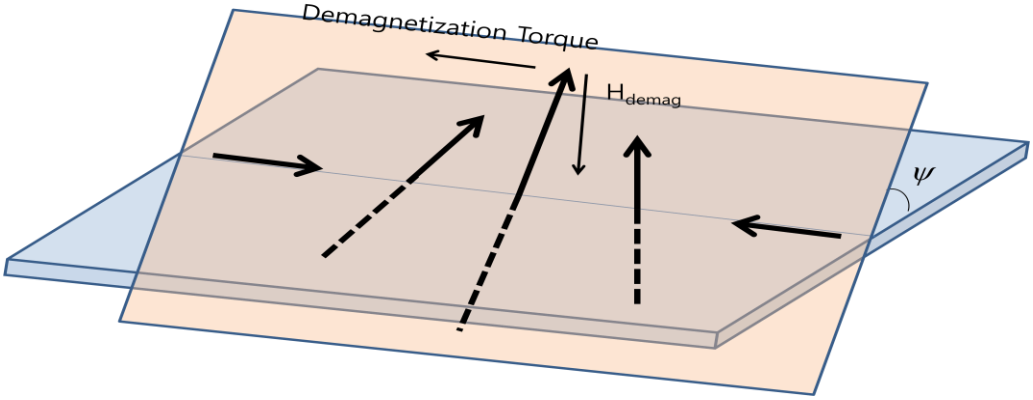


**(B) Effect of Canted Spin Plane**

**Figure 2.3 Schematic of Spin Distribution in TW confined to 1-D Nanowire**

1-D transverse wall gives the simplest model of domain-wall propagation and Walker breakdown phenomenon. Consider the TW confined on 1-D wire. Applied field and spin in TW generates the perpendicular field torque [Fig 2.3(A)]. Because of this torque, spin plane rotates out of sample plane (called canting angle $\psi$) and demagnetization field (corresponding torque) is generated. This demagnetization torque cants the DW spin towards the applied fields [Fig2.3(B)]. At high fields, $\psi$ rotates suggesting full precessional motion.(Walker breakdown).

## 2.4 Landau Lifshitz Gilbert (LLG) equation

Dynamic micromagnetics predicts the time evolution of the magnetic configuration of a sample subject. Landau and Lifshitz[8] introduced the basic dynamical equation which describes the time evolution of magnetizations, and Gilbert introduced a more convincing form for phenomenological damping. The combined form of these two is the LLG equation.

**(a) Single spin dynamics**

A free electron spin angular momentum operator S under the time dependent external magnetic field can be described by the Zeeman term,

$$H_S = -\frac{g\mu_B}{\hbar}\mathbf{S}\cdot\mathbf{B}(t),\ \mathbf{B}(t) = \mu_0\mathbf{H}(t), \tag{2.6}$$

where $g$, $\mu_B$ and $\mu_0$ are the gyromagnetic ratio, Bohr magneton and permeability in vacuum, respectively. The Schrödinger equation and angular momentum commutation relations deduce the expectation value of the spin operator satisfy the dynamical equation,

$$\frac{d}{dt}\langle\mathbf{S}(t)\rangle = \frac{g\mu_B}{\hbar}\langle\mathbf{S}(t)\rangle\times\mathbf{B}(t). \tag{2.7}$$

Magnetization is defined as

$$\mathbf{M} = \frac{g\mu_B}{\hbar}\langle \mathbf{S} \rangle \equiv \gamma \langle \mathbf{S} \rangle, \text{ where } \gamma = \frac{g\mu_B}{\hbar}. \tag{2.8}$$

Then unit volume magnetization M is described by evolution equation,

$$\frac{d\mathbf{M}}{dt} = -\gamma_0 [\mathbf{M}(t) \times \mathbf{H}(t)], \quad (\mathbf{B} = \mu_0 \mathbf{H}, \gamma_0 = \mu_0 \gamma). \tag{2.9}$$

Experimental hysteresis curves of ferromagnetic material show the saturation after critical point because of damping term mentioned by Gilbert. Thus Eq. 2.9 is rewritten with Gilbert damping and normalization,

$$\begin{aligned} &\mathbf{m}(t) = \frac{\mathbf{M}(t)}{M_S}, \\ &\frac{d\mathbf{m}}{dt} = -\gamma_0 [\mathbf{m} \times \mathbf{H}] + \alpha \left[ \mathbf{m} \times \frac{d\mathbf{m}}{dt} \right], (\alpha = \lambda \gamma_0, \lambda << 1), \end{aligned} \tag{2.10}$$

where $\lambda$ is a damping parameter. Eq. 2.10 is the simplest LLG equation form which describes a dynamics of a single spin under the applied field $\mathbf{H}(t)$.

**(b) Generalized LLG with adiabatic and non-adiabatic spin-transfer-torque**

LLG equation represents dynamics of spin in a ferromagnetic thin film under the spin current. Spin polarized current transfer the spin angular moment to the film. This is called spin torque effect.

The generalized version of LLG equation[9] with spin torque terms is

$$\frac{\partial \mathbf{m}}{\partial t} = -\gamma_0 [\mathbf{m} \times \mathbf{H}_{eff}] + \alpha [\mathbf{m} \times \frac{\partial \mathbf{m}}{\partial t}] - v_j \frac{\partial \mathbf{m}}{\partial x} - \beta v_i \mathbf{m} \times \frac{\partial \mathbf{m}}{\partial x}. \tag{2.11}$$

The first term comes from the effective field which include applied, demagnetizing, anisotropy, and exchange field. The second term is Gilbert damping term already mentioned. The third term describes adiabatic spin torque. The conduction electron spin is affected by domain wall when it is passing through the wall, and the effect changes the local magnetization and electron spin magnetic moment is parallel to the local

magnetization direction. This spin torque flips spin direction as it crosses the domain wall. The adiabatic process transfers electron spin angular momentum to the local angular momentum within the wall region atom through exchange interaction. The last term is non-adiabatic term, its origin and magnitude is still unclear. The coefficients of both spin-torque terms are linear functions of the current density $J$, and therefore do not allow non linear response. Momentum transfer, spin-mistracking, and spin-flip scattering are proposed candidates of this non-adiabatic term. [10] Thus, this term is determined by experiments.

## 2.5 One dimensional model of domain wall dynamics

The 1D model of DW propagation can be used to obtain a pair of coupled equations[11]:

$$\dot{q} = (2\pi M_s)\gamma\Delta \sin 2\psi + \alpha\Delta\dot{\psi} + \eta u. \tag{2.12}$$

$$\dot{\psi} = \gamma H_a - (\alpha/\Delta)\dot{q} + (\beta u)/\Delta \tag{2.13}$$

In Eq. 2.12, $M_s$ = saturation magnetization, $\gamma$ = gyromagnetic constant, $\alpha$ = gilbert damping constant, $\eta$ = adiabatic contribution, $\gamma$ = non-adiabatic contribution, $\Delta$ = wall width, and effective electron velocity parameter $u = -\left(\frac{g\mu_B p}{2eM_S}\right)j$ where $g$ =Landé factor, $\mu_B$ = Bohr magneton, $p$ = spin current polarization, $j$ = current density. This pair of equations has well known solutions at two limits ,

$$\dot{q}_{low} = \frac{\gamma\Delta}{\alpha}H_a + \frac{\beta u}{\alpha} \quad , \qquad \dot{\psi} = 0 \tag{2.14}$$

$$\dot{q}_{high} = \gamma\Delta\alpha H_a + \eta u \qquad \dot{\psi} >> 1. \tag{2.15}$$

In low field region ($\dot{\psi} = 0$), $\psi < \frac{\pi}{4}$ and the wall propagates at a uniform velocity. In high field region ($\dot{\psi} >> 1.$), $\psi > \frac{\pi}{4}$ and the demagnetization torque is decreased and became negative during the precession cycle. As a result, small net damping torque cants the spins toward the applied field with oscillation, and average velocity drops greatly. This phenomenon appears on a mobility curve. Linear graph drops at certain point (Walker breakdown field), and it increases linearly again (but the slope is much smaller). The 1-D model describes the DW mobility as the sum of field-driven and current-driven contribution in the two regions of linear response.

$$v(H, j) = \mu_H (H - H_0) + \mu_j (j) \tag{2.16a}$$

where

$$\mu_H = \frac{\gamma\Delta}{\alpha}, \mu_j = \frac{\beta P \mu_B}{eM_S} \qquad (H < H_W), \tag{2.16b}$$

$$v = \frac{\gamma\Delta H_a}{\alpha} + \frac{\beta u}{\alpha} - \frac{\gamma\Delta}{\alpha(1+\alpha^2)}\sqrt{(H_a + (\beta - \alpha\eta)u/\gamma\Delta)^2 - (H_W)^2}$$

$$\mu_H = \frac{\alpha\gamma\Delta}{1+\alpha^2}, \mu_j = \frac{(\eta + \alpha\beta)P\mu_B}{(1+\alpha^2)eM_S} \qquad (H >> H_W), \tag{2.16c}$$

$$\Delta = \pi\sqrt{A/(2\pi D_y M_S^2)}.$$

Material specific parameter, $H_0$, is a phenomenological constant (coercive field), $A$ and $M_S$ are the exchange constant and saturation magnetization, $\alpha =$ Gilbert damping constant and $P =$ conduction electron spin polarization. The symbols, $\gamma, e$, and $\mu_B$ represent the gyromagnetic ratio, electron charge and Bohr magneton, respectively. Spin-torque models postulate “adiabatic” and “non-adiabatic” interactions between spin-polarized electrons and DW spins, and the spin-torque model parameters $\beta$ and $\eta$ characterize the strength of nonadiabatic and adiabatic spin torque. The parameter $\Delta$ characterizes the DW width and $D_y$ is the transverse demagnetizing factor.

## 2.6 Barkhausen Jump

Domain-wall displacements occur in two basic regimes: a hydrodynamic regime in which walls move in a continuous way described by a mobility function $v(H)$, and in a regime characterized by a succession of discrete displacements called Barkhausen jumps. The nanometer-scale samples, that can be used to explore domain-wall dynamics and spin-torque effects, also exhibit Barkhausen effects at low applied field sweep rates, and the Barkhausen regime offers interesting opportunities for studying spin-torque effects when the Barkhausen jumps are stimulated by electric current pulses[12]. Barkhausen effects in magnetic nanostructures also offer a broad range of scientific opportunities for probing stochastic effects in low dimensional (1D and 2D) systems. Therefore, a brief review of selected Barkhausen phenomena and scientific issues are presented.

The Barkhausen Effect (BE) is a discontinuous change in magnetization of a sample. Heinrich Barkhausen discovered this effect when he magnetized iron because the iron is not magnetized uniformly. The magnetization occurred in random steps, and these steps didn't correspond to the size of a single iron atom. Before the domain wall scanning skill developed, BE was treated as indirect evidence of domain wall hypothesis which was mentioned by Weiss. BE can be easily described by hysteresis loop. Domain wall interacts with lattice defects, impurities, surface and interface roughness. These components affect pinning of domain-wall motion. It's complex to consider all these factors, but phenomenological magnetic hysteresis simply gives BE jump-amplitude distribution functions and various scaling laws. .

.

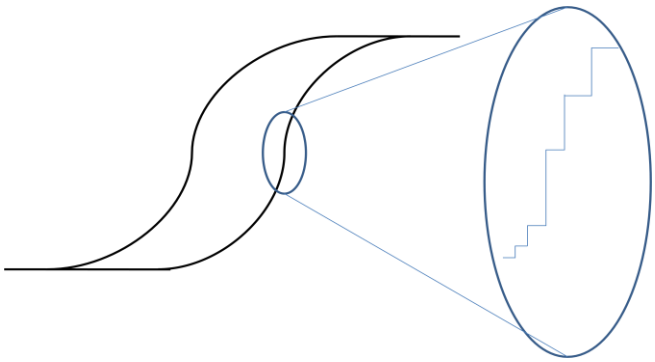

**Figure 2.4 Conceptual Image of Barkhausen Jump in Hysteresis Loop**

The DW motion under uniformly changing applied field can be analytically interpreted by ABBM model.[13] This model gives scaling functions for jump probability amplitude P.

$$P(\upsilon) = \upsilon^{-\alpha} f(\upsilon/\upsilon_0) \qquad \alpha = 1 - c, \tag{2.17}$$

$$P(\Delta M) = (\Delta M)^{-\beta} f(\Delta M / \Delta M_0) \qquad \beta = 3/2 - c/2, \tag{2.18}$$

$$P(\Delta\tau) = (\Delta\tau)^{-\gamma} f(\Delta\tau/\tau_0) \qquad \gamma = 2 - c, \tag{2.19}$$

where $c \propto dH/dt$ is dimensionless parameter which characterizes the sweep rate and $f$ is cutoff function, and $\upsilon_0, \Delta M_0, \Delta\tau_0$ are material dependent parameters.

# Chapter 3: Sample Preparation: Rectangular Microstructure

## 3.1 Overview

Samples are prepared through complex steps. The first step is Si wafer cutting and cleaning. The second step is photolithography for Ta/Py/Ta depositions. The third step is three layers sputtering deposition. The fourth step is lift-off process. The fifth step is trimming of pattern shape by using FIB. The sixth step is magnetic force microscope (MFM) scanning to identify the domain wall shape and measure the height of Ta/Py/Ta layers. The seventh step is photolithograph for Au electrodes. The eighth step is Au deposition. The last step is second lift-off process. Each step is explained in following chapters.

## 3.2 Photolithography

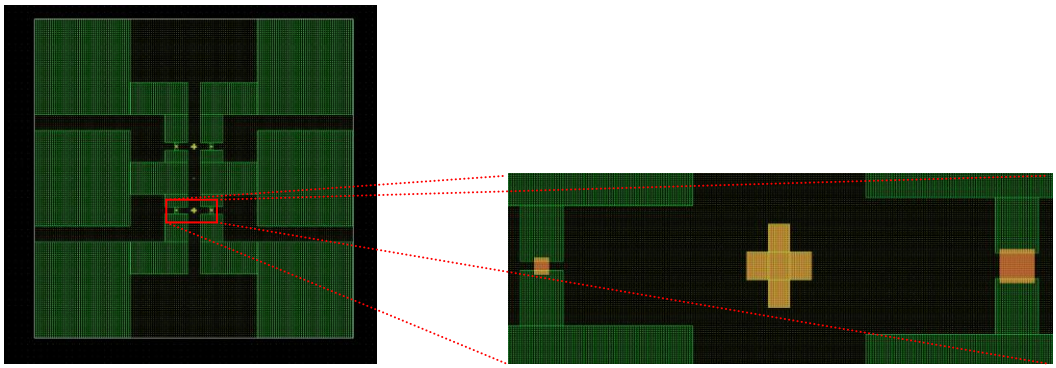

**Figure 3.1 Photolithography Mask**

Prototype experiment is not included in this thesis. In that experiment, macroscopic pattern was made by using a slit.(contact mask). The slit was put on the Si wafer during the sputtering process. That sample surface has a curved surface because of the slit thickness and the gap between slit and Si substrate.(shadow effects). Photolithograph method solves these problems. Two photo-masks are designed, one for Ta/Py/Ta layers, the other for the Au electrodes. In Fig. 3.1, green parts are Au electrode parts, orange parts are three layers(Ta/Py/Ta) deposition parts, and cross shapes (green

and grange overlapped part) were made for mask aligning. Each rectangular shape size is $30\mu m \times 38\mu m$ , $30\mu m \times 34\mu m$ , $60\mu m \times 70\mu m$ , and $60\mu m \times 80\mu m$ . (Trimmed rectangular structures are $20\mu m \times 28\mu m$ , $20\mu m \times 24\mu m$ , $50\mu m \times 60\mu m$ , and $50\mu m \times 70\mu m$. The observed domain-wall pattern depends on the sample structure size and thickness, and this size set gave a clear closure domain pattern in this deposition thickness [Ta(4nm)/Py(20nm)/Ta(4nm)]. Bigger rectangular was made because the spare parts give a room for safety mask aligning, and FIB trimming process can control the extra area.)

*Photolithography Recipe*

1. Si wafer is sonicated by acetone and rinsed with ethanol, IPA(Isopropanol) and de-ionized(DI) water. The wafers were dried by $N_2$ blow gun for the each step. This process eliminates organic contamination (Acetone sonic process), chemical contamination (IPA and DI water process) and dust.
2. Cleaned Si wafer is coated with Photo Resist S1818 by the Laurell Technologies Spincoater (4000RPM for 1min).
3. Suss MA6 Mask Aligner exposes the 350W ultra-violet (UV) for 12s for the machine Intensity 6.5 case (The multiple of exposure time and machine intensity number (changeable value) should be constant to keep the same exposure condition.)
4. The sample is developed by MF Neg319 for 45s.

This developed sample is ready for three layer sputtering deposition.

After the FIB trimming step, the second photolithography is needed for Au electrode deposition. Cleaning and photoresist coating are prepared exactly same as the previous steps. On the sample holder of the mask aligner, the cross align mark on the

sample and the cross mark on the photo mask should be aligned and exposed for Au deposition. Same developer and developing time is used as before. This sample is ready for the Au thermal deposition.

### 3.3 Deposition

To explore sample shapes and sizes that produced a closed domain wall structure (Landau state domain wall pattern), the sample size and thickness was varied systematically.

- Contact mask deposition experiments yielded comprehensive background for milling the isolated rectangular structure. The macroscopic wire was easily deposited by using 50μm x 3mm slit masks. This macroscopic wire has gentle curvature because of slit mask thickness and tiny gap between slit mask and sample, but the thickness variation of the wire is less than 2nm near the central axis (within 10μm). Photolithography method is introduced to solve this problem.
- Sample on the glass was melted by joul-heat during the high current flowing. Si wafer has better heat conductivity, and this can lower the sample temperature. The Ta(4nm)/Py(20nm)/Ta(4nm) layers were deposited on a 370μm thick substrate of thermally oxidized Si(100) at the room temperature.

Permalloy film is deposited by RF sputtering, tantalum capping layer is deposited by DC sputtering. This three layer films are deposited by Cook Ebeam/Sputter Deposition system. This deposition system is equipped with Ebeam evaporator, RF sputter, and DC sputter.

In deposition chamber, the developed sample is mounted on rotatable disk sample holder (sample is facing down to the target). The disk sample holder can be rotated to the vertical position of the sputtering target. Usually the films are deposited at $10^{-6}$ Torr level because higher pressure can make oxide layer on the sample surface. After baking the chamber overnight, the base pressure can reach to $10^{-7}$ Torr. During the sputtering, Ar partial pressure was $1 \times 10^{-2}$ Torr. Ever present free electrons are accelerated away from the target cathode to substrate anode. These electrons collide to Ar atom, and Ar+ is generated. The Ar+ is accelerated to negatively charged target, and their collisions blast target material, and additional free electrons pop up. The additional electrons continue to maintain the plasma (Ar+, e-). Some free electrons combine with ion, and release the photons which glow the plasma. Blasted target material is deposited on the substrate. In DC sputtering, the target must be conductive. Otherwise the target surface will charge up with Ar+ ions which repel other Ar+, and this repulsive interaction would stop the sputtering process.

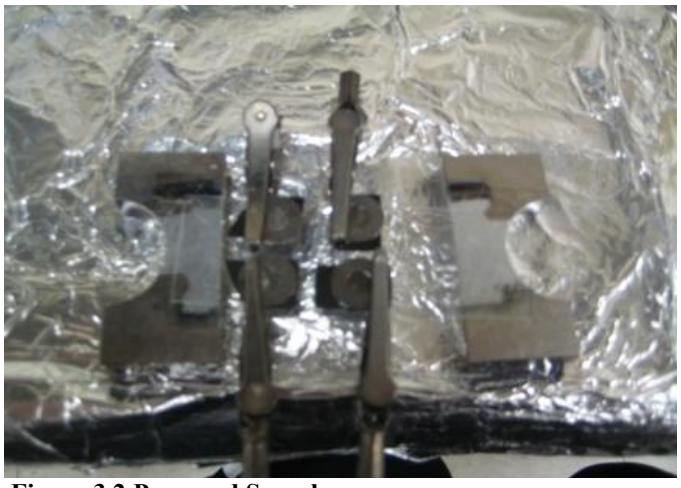

**Figure 3.2 Prepared Sample**

Following is recipe of sputtering process.

1. Developed sample should be cleaned, and this sample wafer is fixed on the microscope slide [Fig. 3.2]. Usually 4 samples can be mounted on the one microscope slide. Overall sample mounting area should be compact compared to the target size for uniform deposition.

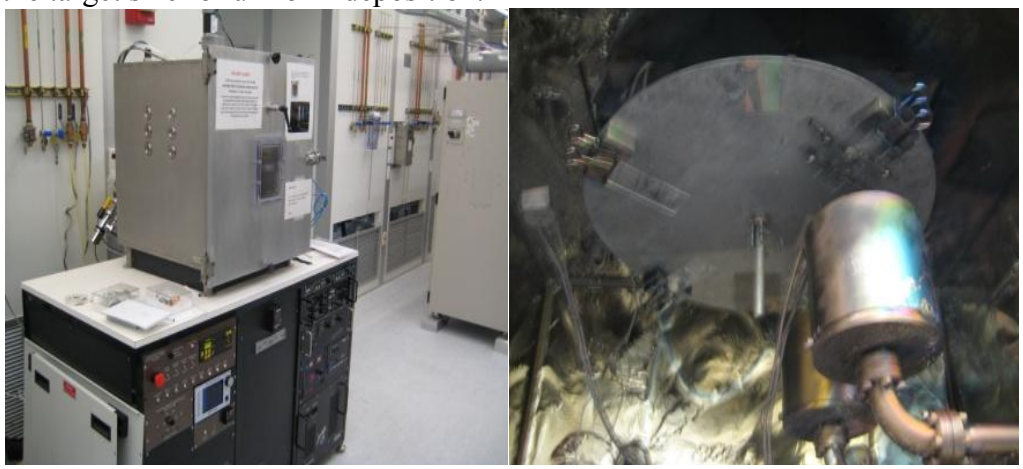

**Figure 3.3 Cook Ebeam/Sputter Deposition System**

2. This sample is mounted on the rotatable disk sample holder in the chamber, and Ta and Py targets are put on the sputtering heads.
3. Base pressure should be lower than $10^{-6}$ Torr. Otherwise, oxygen can be deposit with sputtering source. Chamber also should be baked over 140$^{\circ}$C for reducing water vapor partial pressure, and should be cooled down to the room temperature.
4. Before starting the sample deposition, pre-deposition process is required to stabilize the sputtering condition and to clean the sputtering targets. The growth rate shown by the crystal thickness monitor is untrustworthy, but the stable growth rate guarantees the stable sputtering condition. Deposition condition for the sample thickness can be found from the test experiment. Actual deposited sample thickness can be measured by AFM after the whole deposition process.

5. After the chamber is stabilized, Ta(4nm) was deposited on the sample to make the bottom capping layer. The growth rate depends on Ar partial pressure and power of DC sputtering process. Ar flow rate is 50scc/m (standard cubic centi-meter: $cm^3/min$ at 1atm, $0^{\circ}C$). The sputtering power needs to be minimized for fine control of the sample thickness (30 watt is used, and Ta is deposited for 15s to make 4nm of Ta layer).
6. Permalloy was also deposited after another test glass deposition step. RF deposition rate is controlled by sputtering power and Ar partial pressure. The display of the sputtering system shows the reflectived power and this value should be minimized. Impedance matching process automatically minimized the reflectived power. But this automatic impedance matching process can choose a local minimum instead of the global minimum. Therefore, the deposition condition can be changed, depending on a local minimum, and, in this case, the automatic matching process should be controlled manually to minimize the reflective power. Py(20nm) was deposited at the 50 incident power for 5min 30s.
7. The top capping layer of Ta is required to prevent the Py oxidation. This top capping process is same as the step 5.

These three-layered samples were scanned by AFM for the surface morphology and thickness estimation. Resistance test is the simply second best way for thickness estimation .

Au electrode is deposited after this sputtering deposition process and FIB milling and second photolithography. The electrode [Cr(10nm)/Au(50nm] was thermally deposited [Fig. 3.4].

**Figure 3.4 Thermal Deposition Chamber**

## 3.4 Focused Ion beam milling

Focused ion beam milling is used for the sharp edge trimming. Long milling time can shift the milling position, thus single milling process should be shorter than 20 minutes, while low ion beam intensity is preferred for the sharp edges. These two conditions contradict with each other. Thus, two steps milling is used to satisfy both condition. In this experiment, 300pA ion beam is used for the rough outline milling, and 30pA ion beam for the fine boundary. The milling depth should be calibrated under 20 nm-milling setting of Si, corresponding to the actual 50nm milling of Py.

# Chapter 4: Sample Characterization by MFM and DC Resistance

## 4.1 MFM characterization/Domain patterns

Veeco MultiMode SPM, the commercial tool, is used for the magnetic DW and morphology characterization and thickness estimation of the samples. Model MESP probe tip can support both atomic force microscopy(AFM) and magnetic force microscopy(MFM) functions. AFM scans the morphology of sample surface by two methods, contact mode and tapping mode. The tip is dragged on the sample surface in the contact mode, and measures the surface by analyzing the feedback signal to maintain the tip cantilever deflection due to the atomic force between tip and sample. This mode is fast and accurate, but exerts high lateral force on the sample. Tapping mode uses oscillating cantilever during the scanning. The cantilever tip touches sample only for a short time, solving the lateral force issue. MESP probe tip supports the tapping mode, and this scanning is used to check the nanowire thickness and pattern. MFM can be used to characterize the magnetic configuration of the sample, especially the domain wall pattern. The ferromagnetic film coated tip acts as magnetic dipole and interact with the stray fields from domain walls. High magnetic moment tip strongly interacts with the magnetic sample, and signal-to-noise ratio is high. However, it can drag the domain wall during the scanning. For our Py samples, carefully chosen MESP tip's magnetic moment is $1\times 10^{-13}$emu.

Permalloy is a soft ferromagnetic material, and magnetic probe tip can drag the wall slightly (even though we used a low magnetic moment tip). Helmholtz coils (electromagnet) is used to apply an external magnetic field during the scanning. The magnet is powered by Kepco bi-polar amplifier which is connected to computer with a D/A card. The maximum field of this magnet is about 50 Oe.

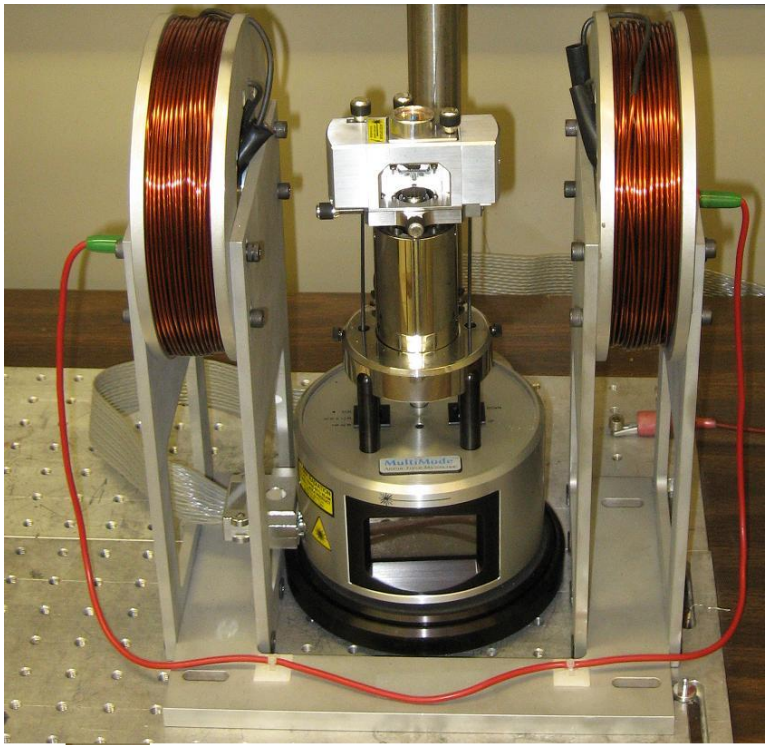

**Figure 4.1 Magnetic Force Microscope Setup**
MFM head locates at the center of Helmholtz coils (electromagnet), which is used to apply an external magnetic field during the scanning. The power is provided by Kepco bi-polar amplifier. The maximum magnetic field is around 50 Oe, which is enough to drive the domain wall in micro magnetic structures.

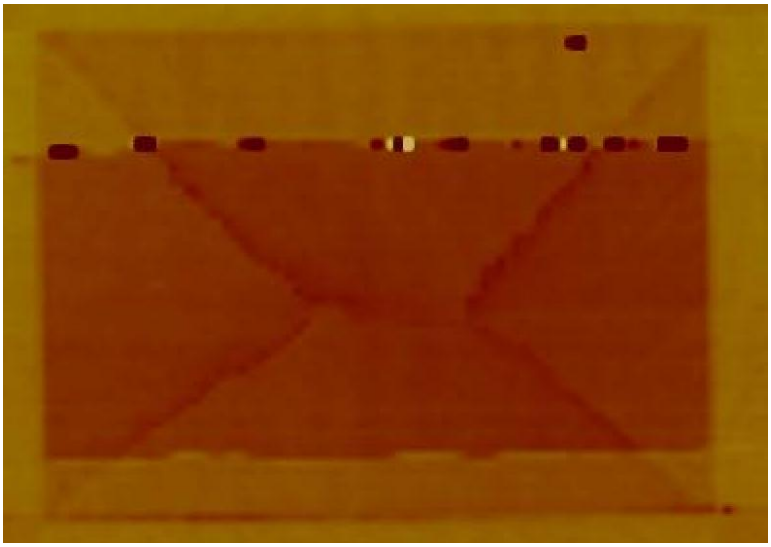

**Figure 4.2 MFM Image of Rectangular Sample ($20\mu m \times 28\mu m \times 20nm$) Showing Simple Closure Domain Structure**

Figure 4.2 shows the scanned MFM image of the rectangular sample of $20\mu m \times 28\mu m \times 20nm$ (sample #3 in Table 1) at the zero magnetic field. The observed domain wall structure shows the Landau state pattern, which is a stable domain wall configuration for the given geometry. The upper and lower parts of the image show the gold electrodes, which don't affect the magnetic structure of Py layer. The observed domain wall patterns highly depend on the sample geometry and sample quality. Some samples exhibit complex domain wall patterns, such as double or triple Landau pattern. This sample is suitable for studies of DW mobility asymmetry under conditions in which electric current stimulates a Barkhausen jump.

# Chapter 5: Experimental Results

The magnetic-field driven hysteresis loops and Barkhausen jumps studied in experiments described in this chapter are initial experiments required to characterize dynamic magnetic response. Future experiments will add electric current stimulated and driven effects related to the spin-transfer torque interaction.

## 5.1 Magneto optic Kerr effect

The light source of the experiment is a single longitudinal mode solid state laser (Crystal laser) with 658nm wave length and 50mW power. It has significantly smaller noise level than old He-Ne gas laser. The laser is polarized by a Glan-Taylor prism polarizer with extinction parameter of $10^{-5}$, and the polarization direction is vertical to the table(s polarization). The polarized beam passes through the $\times 10$ beam expander. which expands the beam to the size of focusing lens, because larger numerical aperture is needed for smaller focus point on sample. Iris cuts the outer part of beam which is not highly uniform. Focusing lens is Mitutoyo M Plano Apo $\times 10$ objective lens, which has 0.28 numerical aperture, 20mm focal length, and 34mm working distance. The incident beam angle is $45^0$ to the sample surface, and the beam shape on the sample will become elliptical. The minimum length of the ellipse major axis is about 2μm (Gaussian half maximum width).

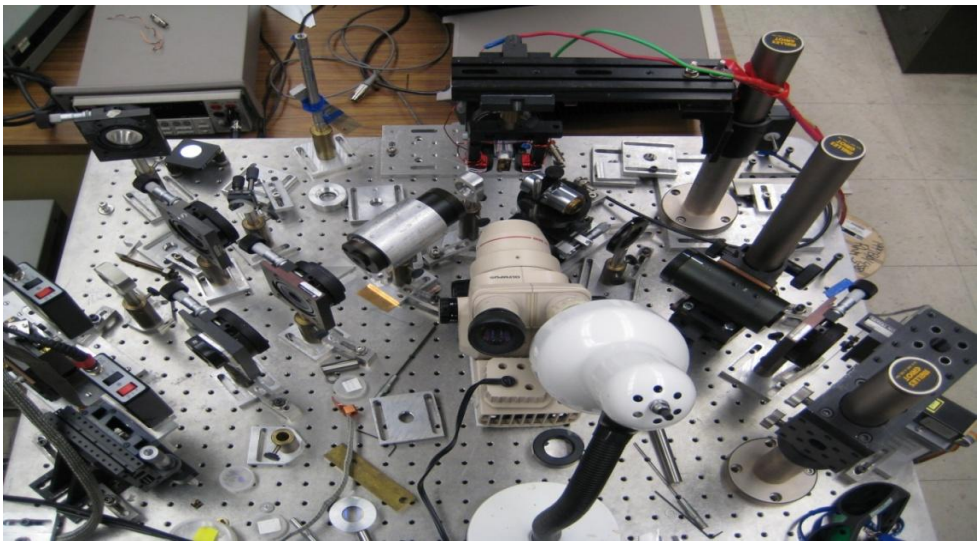

**Figure 5.1 MOKE Polarimeter**

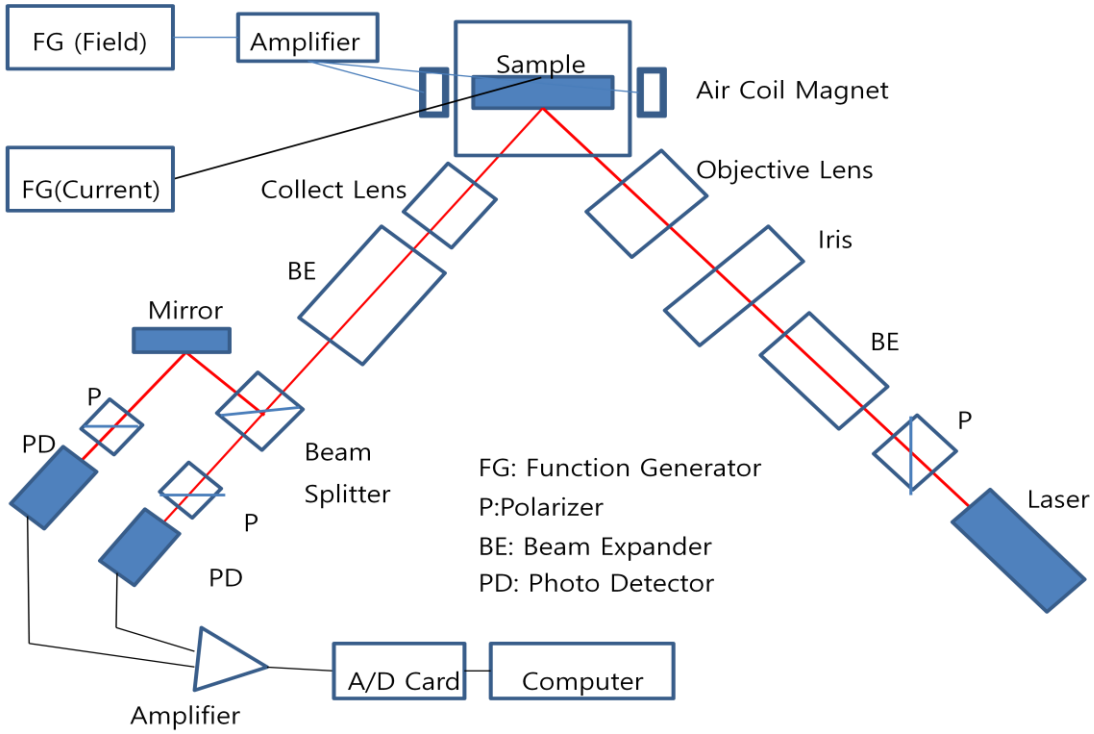


**Figure 5.2 Schematic Diagram of MOKE Polarimeter**

Sample is mounted on the 3-axis manual sample stage which controls the sample position. The reflected beam passes through the plain-convex lens becomes parallel to

optical axis, and inversely installed $\times 20$ beam expander controls reflected beam size. MOKE rotation signal can contain mechanical vibration noise, and beam splitter and differential detection is used for noise-eliminating process. 50/50 non-polarizing beam splitter divides the beam. One of split beams travels through the Glan-Taylor polarizer with polarizing angle $+\emptyset$, and the other beam travels through the other Glan-Taylor polarizer with polarizing angle $-\emptyset$. The difference between these two polarized beam intensities makes the differential signal. This beam split process remove the noise from the any mechanical vibrations and laser source noise. The photo detector is Model 1621 Visible Nanosecond Photo detector. The output of each photo detector is differentially amplified by Stanford Research System Low-noise pre-amplifier Model SR560. High bandwidth gives high temporal resolution, but it also gives high frequency noise. Therefore, fine bandwidth control is important to obtain the desired signal-to-noise ratio.

The maximum field of this magnetic system is about 40 Oe. Air coil is required for excluding the remanent field effect, and Helmholtz coils is used as magnet. This Helmholtz coil is driven by a Kepco power amplifier which is controlled by Stanford Research System DS345 (Bandwidth 30MHz).

### 5.1.1 Alignment

Beam alignment is crucial for this MOKE polarimeter, and the proper setup order is necessary for the fine setting. The first step is to mount the sample on the three axis sample stage and align the magnet. Laser is installed on the empty optical table. Next step is polarizer and beam expander alignment. The beam spot should be located at the center of the optics. And objective focusing lens is mounted on the translation stage to adjust the focusing beam size on the sample. All reflected beam should be collected by the plane

convex lens to maximize the signal, and the reflected beam should be parallel to the optical axis after passing through the collection lens. Beam spot should be centered at the inversely installed beam expander also. Beam splitter should be horizontal, and mirror can control the splitted beam path to the center of the polarizer. And the last step is the detector alignmnet to maximize the MOKE signal. The alignment can be distorted by mechanical and thermal drift of the optics, and periodic maintenance is required.

After the alignment, polarizer angle should be adjusted for best S/N ratio. Both of polarizer P1 and P2 are rotated until beam intensity is minimized. Then P1 is rotated by suitable angle, and then P2 is rotated opposite direction until the output intensity is balanced.

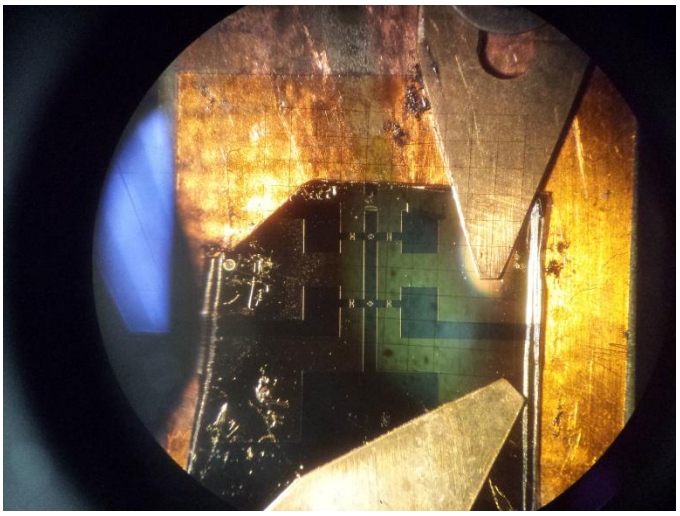

**Figure 5.3 Rectangular Sample Installed on MOKE Polarimeter**

## 5.2 Barkhausen jump measurement and discussion

The sample ( $20\mu m \times 28\mu m \times 20nm$ ) was mounted on the sample stage as shown in Figure 5.3. The triangular sweeping field of 10Hz was applied to the sample. The corresponding maximum field was 12.35 Oe ($dH/dt$=494 Oe/s). The MOKE signals from the detectors were differentially amplified by SR560 low-noise differential amplifier. The

band pass filter setting was 0.3 Hz high-pass filter (6dB/oct) and 3 kHz low-pass filter (6dB/oct), and the gain setting value was around $10^4$. The output signal was captured by GaGeScope digital oscilloscope. GaGeScope software acquired the MOKE signal data during 2000 cycles, and its sampling rate is 50 kHz. 4608 data points are acquired for single cycle. Thus, one cycle of data set covers $\frac{4608}{50000} \approx 0.0921\text{s}$

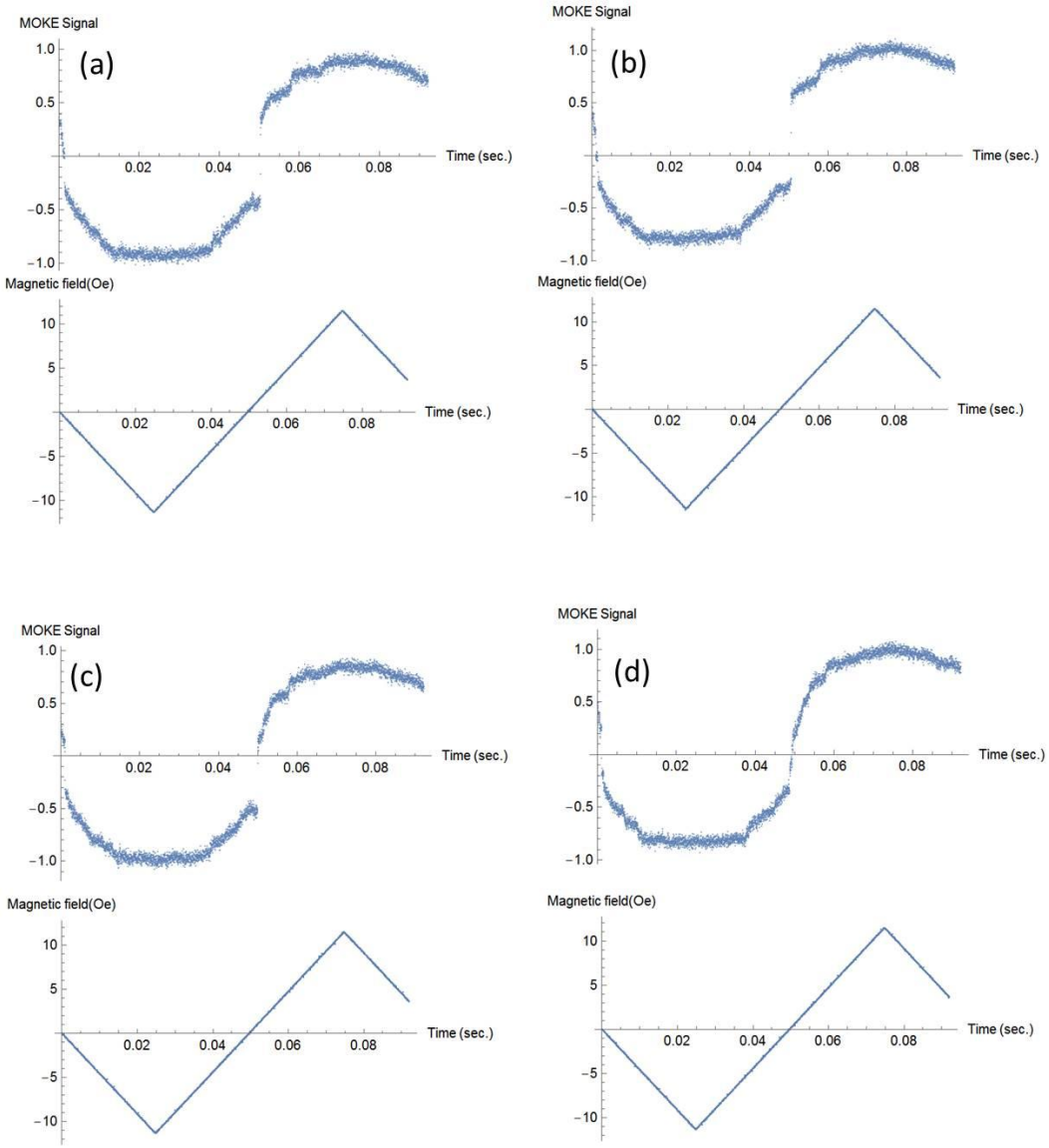


**Figure 5.4 Magnetic reversal transients**

Figure 5.4 shows several sets of single MOKE transient data for the same sample. The sign-to-noise (S/N) ratio of the transient data is around $S/N \approx 2/0.03 = 66.7$. The properties of jumps in Fig 5.4 is that the values if H and M where they occur, along with their amplitude, randomly change form one loop to the next with no apparent correlation. To characterize the statistical properties of the BJ, the amplitude of each jump and the magnetization value are considered. (Eq 2.18) is commonly observed feature, which gives a linear dependence when plotted on a log-log graph. The observed value is range from 1.3 to 1.8 in bulk sample, and 1.6 in continuous thin film.

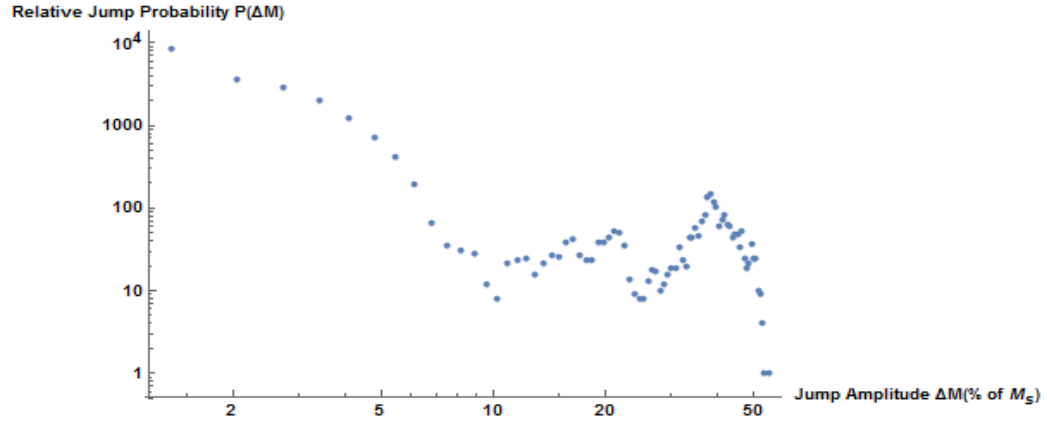


(a) $\rightarrow$ direction.

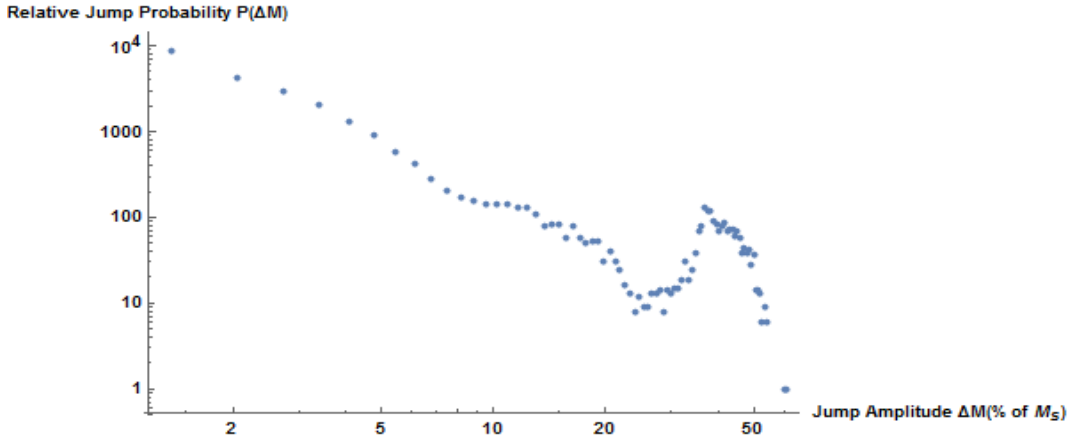


(b) $\leftarrow$ direction

**Figure 5.3 Log-log polts of jump probability vs jump amplitude.**

Magnetic field swap its direction cyclic because it generated by triangular wave. Fig5.3 (a),(b) is jump probability data of each field direction. We can observe Barkhausen jump has direction asymmetry in this sample.

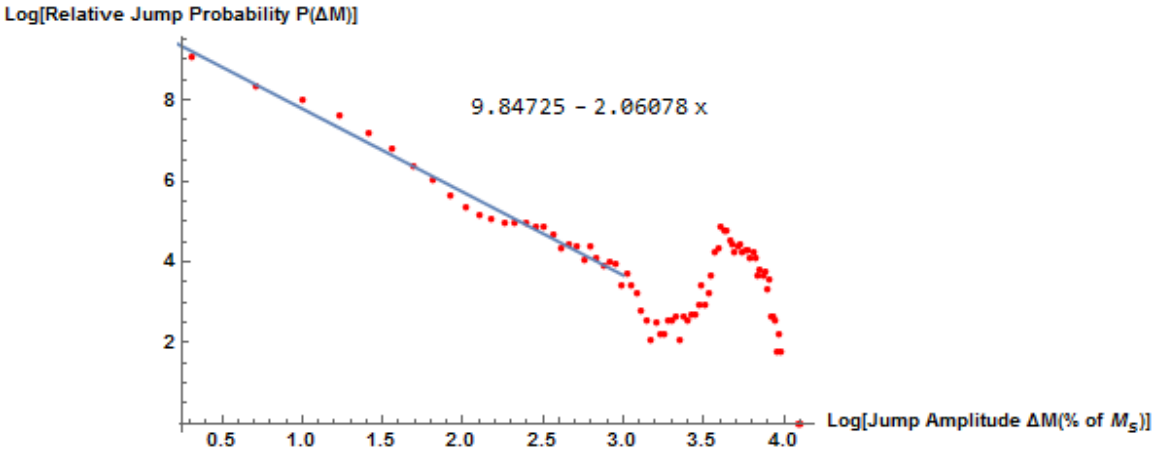


(a) $\rightarrow$ direction

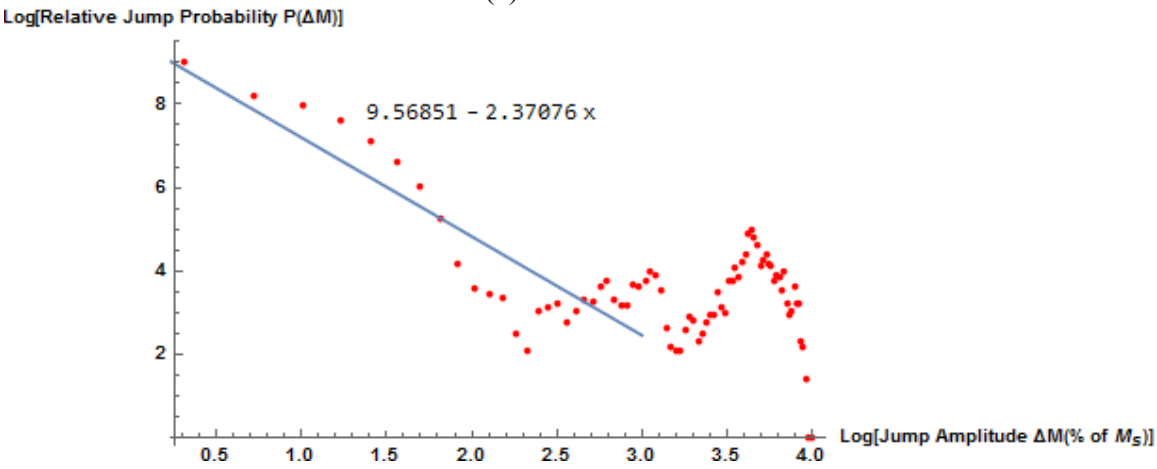


(b) $\leftarrow$ direction

**Figure 5.4 Polts of log(jump probability) vs log(jump amplitude).**

Scaling function (Eq 2.18) can be applied for Fig 5.4 fitting equation.

$\beta = 2.34457$ ($\rightarrow$ direction) , $\beta = 2.22039$ ($\leftarrow$ direction)

There are two differences between Fig 5.4 and other already known graph. The first difference is this graph is not straight line, especially there is well–defined structure for $\Delta M$ between 20 and 50. The second difference is it has short linear line ( $\Delta M < 10$ ), and its slope is steeper. Therefore, this graph gives bigger, and unclear $\beta$ values.

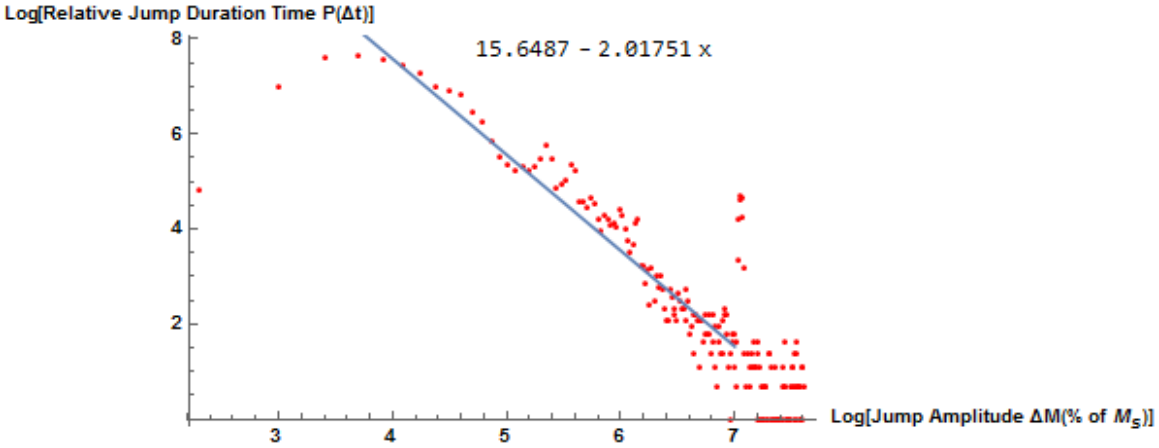


(a) ( $\rightarrow$ direction )

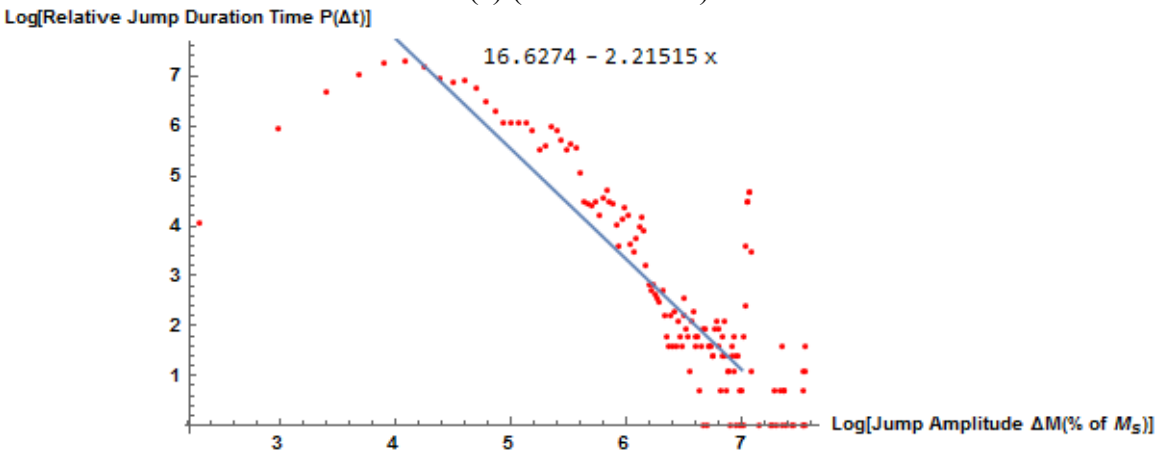


(b) ( $\leftarrow$ direction)

**Figure 5.5 Polts of log(jump probability) vs log(jump duration time).**

Scaling function (Eq 2.18) can be applied for Fig 5.5 fitting equation.

$\gamma = 2.2152$ ( $\rightarrow$ direction), $\gamma = 2.0175$ ( $\leftarrow$ direction)

Theoretical critical exponent were suggest by ABBM model( $\beta = 1.5$ )[14], and CZDS model( $\beta = \frac{4}{3}$ )[15]. Experimental critical exponent were suggest by Shuqiang. (From $\beta = 1.45 \pm 0.05$ to $\beta = 1.0$ as $dH/dt$ is varied from $25 Oe/s$ to $6.3 \times 10^4 Oe/s$ )[16] Ezio Puppin's experimental exponents is $\beta = 4$ with $20\mu m \times 20\mu m \times 80nm$.[17] I used the thinner sample try to remove the thickness effect like eddy current with thinner sample. But scaling parameter still does not match with any the known model and previous experimental result.

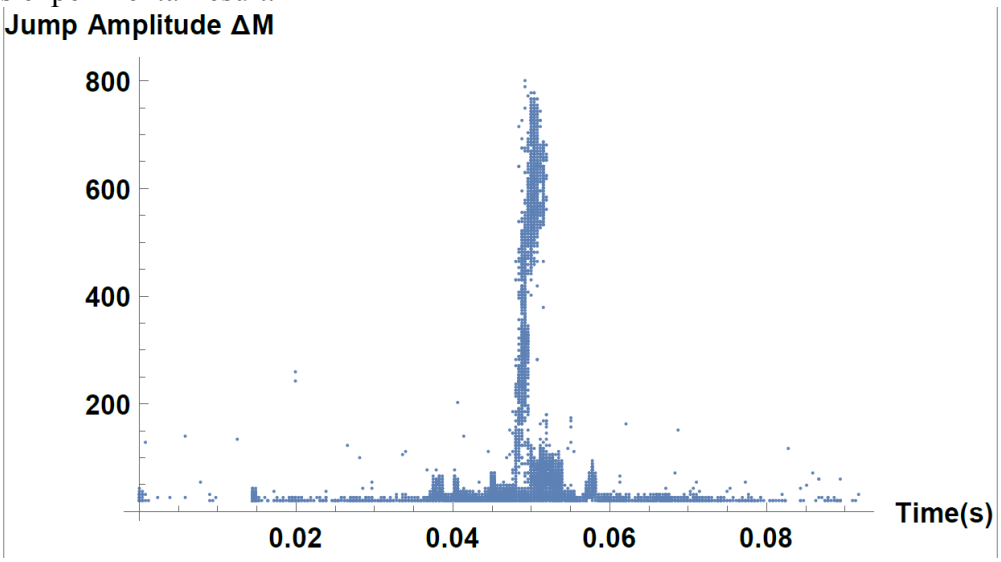


**Figure 5.7 Plot of Jump Probability VS Time**

In summary, experimental critical parameter in compact thin permalloy sample ( $20\mu m \times 28\mu m \times 20nm$ ) is still not matching with theoretical values. Probability amplitude curve is not linear because it has huge bump. Only small range of graph can be analyzed, and acquired experimental parameter is still too big. Fig.5.7 shows high portion of jump happen at 0.05s. This means there are non-random structural jump happen in small sample. However, the sample are suitable for studying current-stimulated Barkhausen transients as demonstrated by Yang[12].

# Chapter 6: Future work on asymmetry of spin-torque effect

## 6.1 Jusang's Ph.D work: Temperature dependence

The nonlinear contribution to $v(H, j)$ varies approximately with $j^2$ in some regions of $H$, but generally appears to be a complex function of $j$ and $H$. The observed $j^2$ component of $v(H, j)$ suggests a contribution from Joule heating arising from the high current density in the nanowire. Thus, Fig 1.2 sample is prepared for experiment and heated during the measurement.

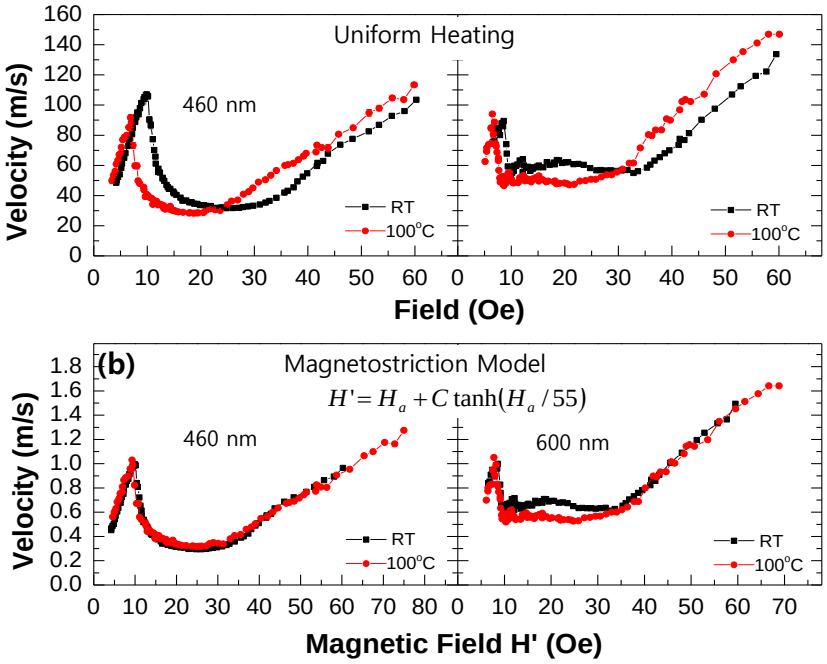


**Figure 6.1 Mobility curves at Room temperature and at $T = 100\ ^{o}C$ for two nanowire width.**

Temperature effects on the DW mobility function were isolated from other linear and nonlinear components in $j$ effects by conducting mobility function studies of uniformly-heated nanowire samples at $j = 0$. Figure 6.1a displays measured mobility curves of 460 nm and 600 nm wide nanowires at room temperature and at $T = 100\,°\text{C}$. The measurements reveal three principal effects of increased temperature: 1) a constant

displacement (due to $\Delta H$ or $\Delta v$ or both) in the mobility curve between 35 and 60 Oe, 2) significant suppression of the double vortex structure (but smaller than produced by $\pm j$ in Fig. 1.2) and 3) a much smaller shift in the mobility curves at applied fields below $H_W$.

Direct temperature-related vertical $(\Delta v)$ and horizontal $(\Delta H)$ shifts in the mobility curve resulting from a 100 °C increase of temperature can be calculated using the 1D model, but these shifts are inconsistent with the experimental results of Fig. 6.1a. The 1D model predicts $H_W = 2\alpha\pi M_S$ and $v_W = 2\gamma M_S \Delta$. For a fixed wire geometry, $H_W$ scales with $M_S$ and $v_W$ scales with $\sqrt{A}$ (both $A$ and $M_S$ decrease with increasing temperature).

Measured behavior of $M_S(T)$ and $A(T)$ based on the temperature-dependent Brillouin light scattering experiments allow estimates of $\Delta H_W(T)$ and $\Delta v_W(T)$ based on the 1D model. The results for $T = 100\,^{\circ}C$ are $\Delta H_W / H_W \cong -10\%$ and $\Delta v_W / v_W \cong -8\%$. Experimental parameters (Fig. 6.1a) for the 600 nm wide nanowire are $H_W = 8\,\text{Oe}$ and $v_W = 9\,\text{m/sec}$, and the model yields $\Delta H_W \cong -0.8\,\text{Oe}$ and $\Delta v_W \cong -7\,\text{m/sec}$. Comparison of the RT and $T = 100\,^{\circ}C$ mobility curves for the 600 nm wide nanowire suggests a valid model would require a significant increase in velocity (examine data in the 30-60 Oe range) or an H-field dependent shift that increases from about 8.5 Oe above $H = 30\,\text{Oe}$. Thus the temperature dependence of $M_S$ and $A$ do not explain the mobility function shift either qualitatively or quantitatively.

## 6.2 Anisotropic stress model

An alternate explanation of the temperature-dependent effects that are apparent in Fig. 6.1a is based on the change in the parameter $H_0$ due to Joule-heating induced

magnetostriction in the Permalloy nanowire $H_\sigma(j^2)$.[18] Magnetoelastic energy in a strained magnetic wire structure is described by [19]

$$\begin{aligned} E_\sigma &= \tfrac{3}{2}\lambda(\sigma_y \sin^2\theta + \sigma_y \cos^2\theta) \\ &= \tfrac{3}{2}\lambda(\sigma_x - \sigma_y)\cos^2\theta + \text{constant}, \end{aligned} \qquad (6.1)$$

where $\theta$ is the angle between the stress axis and magnetization, $\lambda$ is the magnetoelastic parameter for the material, and $\sigma_x$, $\sigma_y$ are the (thermally-induced) stress along orthogonal axes. The mechanical stress, $\sigma_y$, along the Permalloy nanowire axis, and the stress, $\sigma_x$, perpendicular to it were evaluated using the thermal stress module of COMSOL simulation software for the two cases corresponding to Fig.1.2 and Fig.6.1: 1) Joule heating of the nanowire generated by current in the metallic structures, and, 2) uniform heating of the substrate and nanowire by an external source. The change in $H_0$ due to magnetostriction is given by [20]

$$H_\sigma(T) = \frac{E_\sigma(T)}{M_S}. \qquad (6.2)$$

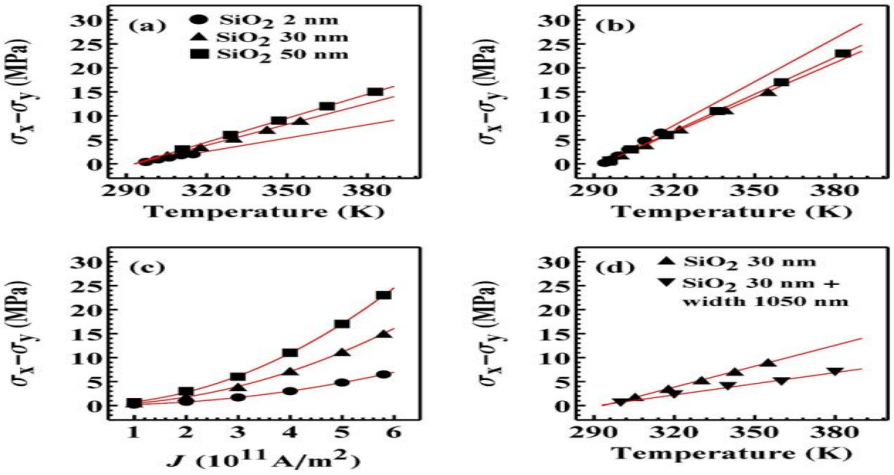


**Figure 6.2 Calculated anisotropic stress in various nanowire structures showing trends in stress function for both Joule heating and uniform heating (as a function of $SiO_2$ thickness). Panel a stress from uniform heating, Panel b temperature increase by electric current Joule heating, Panel c**

**stress as a function of current density, Panel d stress as a function of uniform heating temperature for two nanowire widths.**

Figure 6.2 presents calculated anisotropic stress $(\sigma_x - \sigma_y)$ in the Permalloy conduit for several cases that include variation of the $SiO_2$ layer thickness and the width of the nanowire conduit. The anisotropic stress is reduced by increasing the nanowire width, and is increased significantly for a given value of $j$ for thicker $SiO_2$ spacers due to reduced thermal conduction to the Si substrate through a thicker oxide layer.

Thermoelastic properties of NiFe alloys are complicated by the competition between positive magnetostriction ( $\lambda > 0$ ) for Fe rich alloys and negative ( $\lambda < 0$ ) for Ni-rich alloys (Fig.13-96 in Ref. [19]). The magnetostriction parameter is positive for Ni concentration from 0 to 81 % ( with a null at 30 % Ni) and negative above 81 % Ni (Fig. 6.2a). The magnetostriction parameter is also a function of applied field strength H (Fig. 6.2b).

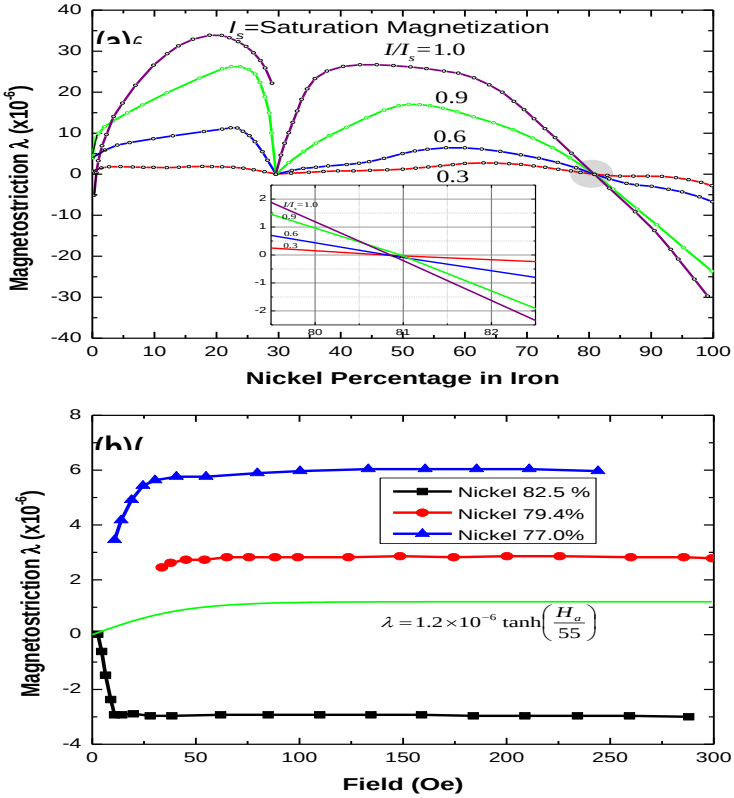


**Figure 6.3. Magnetostriction parameters of NiFe alloys (adapted from Ref. [19]).**

Fig 6.3 presents magnetostriction data of Shulz adapted from Bozorth[19] for Ni-rich Permalloy alloys around 80 % Ni. Examination of the $\lambda(H)$ curve for 80 % Ni of Fig.6.3 shows how the Jolue-heating magnetostriction model can account for the apparent large H field shift of $v(H, j)$ for $H > 30\,\mathrm{Oe}$ and a smaller shift for $H < 10\,\mathrm{Oe}$ apparent in Figs. 1.2 and Fig. 6.1.

A no adjustable parameter calculation of the strain-induced anisotropy field, $H_\sigma(\Delta T)$, at an applied field where $\lambda(H)$ approaches a maximum value for the assumed Ni concentration of the nanowire fails (by factor of 10) to yield the experimental value. However, a one-parameter model achieves an excellent fit to both 460 nm and 600 nm width data for several temperatures as illustrated by Fig. 6.1b. Using parameters Fig.

6.2 and Fig.6.3: $\sigma_x - \sigma_y \approx 160 \times 10^6$ dyne/cm$^3$ at $T = 100\ ^oC$, $\lambda(H) \approx 1.2 \times 10^{-6}$ at $H \approx 60$ Oe and $M_S = 800$ emu, $\Delta H_\sigma \approx 0.4$ Oe. The experimental $\Delta H$ shifts around 60 Oe are approximately 5 Oe. Note that this calculation neglects the direct shifts due to $\Delta M_S(T)$ and $\Delta A(T)$. The inaccuracy is not unexpected: A change in % Ni of 0.6 % (from 80 to 79.4 %) results in over a factor of two increase in $\lambda$, and the experimental data indicate a significant difference measured $\Delta H_\sigma$ (approaching a factor of two) for the 460 nm and 600 nm widths. Additional sources of inaccuracy include possible errors in thickness and width parameters used in the COMSOL calculations, extrapolation from published results for $\lambda(H)$ and bulk parameters used in COMSOL for 20 nm thick samples.

The one-parameter fits of temperature dependent mobility curves shown in Fig. 6.1b were obtained by normalizing the peak velocity at $H_W$ (which accounts for the small $M_S(T)$ and $(\sigma_x - \sigma_y)(T)$ changes, and then using the analytical form of $\lambda(H)$ with an amplitude factor adjusted to yield the best fit for the mobility curve corresponding to a specified nanowire width and measurement temperature. The fitting is very good for both nanowire widths. The model does not account for the temperature dependence of the vortex-antivortex mode that is supported by the 600 nm nanowire in the drive field range extending from 10 to 30 Oe, and the fitting accuracy fails over this region.

## 6.3 Spin-transfer torque parameter

The preceding analysis suggests that the mobility curves displayed in Fig. 1.2 can be more accurately described by adding a second order in $j$ term:

$$\begin{aligned} v(H, j) &= \mu_H (H - H_\xi(H, j)) + \mu_j(j) \\ H_\xi(H, j) &= H_0 + \tfrac{3}{2}\lambda(H)[\sigma_x(j^2) - \sigma_y(j^2)]/M_S \end{aligned} \qquad (6.3)$$

This form of the mobility function preserves the linear in current response of spin-torque models which yield vertical shifts of the mobility curves, and a nonlinear horizontal shift due to the drive-field and temperature ( $j^2$ ) dependence of the coercive parameter. This new physical understanding permits a more detailed analysis of the experimental data in terms of existing spin-torque models. The apparent asymmetry under current reversal is not due to a nonlinear term in the spin-torque model.

The coercivity shift around 30-50 Oe for the 600 nm wide nanowire for $T = 100\ ^{o}C$ is approximately 8 Oe (Fig. 6.1a). COMSOL calculations (Fig. 6.2a and Fig. 6.2c) show that the current densities used in obtaining mobility data in Fig. 1.2 produce anisotropic strain that is essentially the same as calculated for uniform heating at $T \approx 100\ ^{o}C$. Resitance measurements in 600 nm samples at $j \approx 6 \times 10^{11}\ \mathrm{A/m}^2$ suggest nanowire temperature increases of approximately but less than $100\ ^{o}C$. The shift of the $+j$ mobility curve from the $j = 0$ curve around 30-60 Oe is approximately 10 Oe and the shifts of mobility curves at $H_W$ in both Fig. 1.2 and Fig. 6.1 are much smaller (~2 Oe). The experimental data of Fig.1.2 and Fig. 6.1 generally support the model Eq. 6.3.

The 1D analytical model can be used to explore spin-torque model parameter based on the new understanding of experimental data in Fig. 1.2. The spin-torque term (Eq. 6.3) accounts for most of the vertical upward ( $+j$ ) and downward ( $-j$ ) vertical shifts of the mobility curves. Curve fitting exercise can be used to compare spin-transfer-torque model parameters( $\beta$ and $\eta$ in equations 2.16) with theoretical estimates and measured values. The curve fitting results are shown in Fig.6.4.

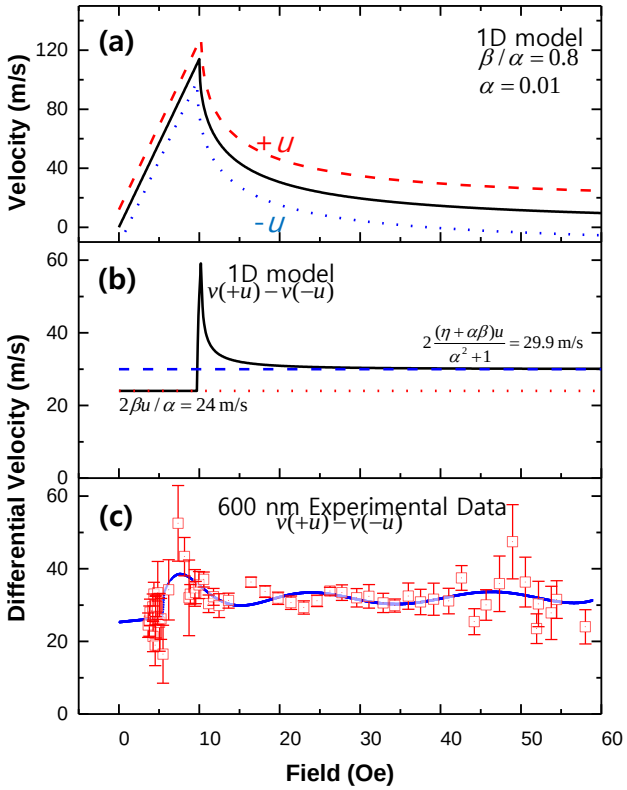


**Figure 6.4 One dimensional model analysis.**

Figure 6.4 displays subtracted experimental data $v(H,+j) - v(H,-j)$ from Fig. 1.2 and corresponding results calculated using the 1D model, Eq. 2.16 (but using the expression for $v(H, j)$ for $H > H_W$ that is not restricted by $H >> H_W$.). The 1D model curves were calculated as a function of spin-torque parameters $\beta$ and $\eta$ using commonly accepted values for Permalloy (i.e., $\alpha = 0.01$) and other constants described in relation to Eq. 2.16. The results are in general agreement with prior work.

## 6.4 Conclusions

The anisotropic stress model appears to accurately explain and account for the experimentally-observed nonlinear effects in the current-driven mobility function. The apparent nonlinear shifts of mobility curves result from anisotropic stress induced by Joule heating. The new understanding of the $J^2$-dependent shifts allow a more accurate and meaningful experimental determination of spin-transfer torque parameter for permalloy.

While a single-parameter fit of experimentally-determined temperature-dependent shifts of mobility curves, based on the anisotropic stress model, provides an excellent account of the temperature-dependent shifts, numerical simulations fail to predict the correct magnitude of the shift. Additional experiments on samples with accurately-characterized composition are needed to explore the problems with the numerical simulation.

# Bibliography


1. G. S. C Beach, C. Kustson, C. Nistor, M. Tsoi, and J. L. Erskine, *Phys. Rev. Lett.* **97**, 057203 (2006).
2. M. Hayashi, L. Thomas, Y.B. Bazaliy, C. Rettner, R. Moriya, X. Jiang, and S.S.P. Parkin, *Phys. Rev. Lett.* **96**, 197207 (2006).
3. C. Nistor, G. S. D. Beach, and J.L. Erskine, *Rev. Sci. Instrum*. **77**, 103901 (2006).
4. G. S. D. Beach, C. Nistor, C. Knutson, M. Tsoi, and J.L. Erskine, *Nature Materials* **4**, 741 (2005).
5. Soshin Chikazumi, *Physics of Ferromagnetism*, Oxford University Press, Oxford, 1997.
6. Michael P. Marder, *Condensed Matter Physics*, John Wiley & Sons, New York, 2000.
7. Charles Kittel, *Introduction to Solid state Physics, 6th Ed*, John Wiley, 1991, P.454.
8. L. D. Landau and E. Lifshitz, *Phys. Z. Sowjetunion* **8**, 153-169 (1935).
9. A. Thiaville *et al*., *Europhys. Lett*. **69**, 990 (2005).
10. C. Burrowes, A. P. Mihai, D. Ravelosona, J.-V. Kim, C. Chappert, L. Vila, A. Marty, Y. Samson, F. Garcia-Sanchez, L. D. Buda-Prejbeanu, I. Tudosa, E. E. Fullerton, and J.-P. Attané, *Nature Phys*. **6**, 17 (2010).
11. H.-B. Chen and Y.-Q. Li, *Applied Phys*. **9**, 7 (2016).
12. S. Yang and J. L. Erskine, (unpublished).
13. B. Alessandro, C. Beatrice, G. Bertotti, and A, Montorsi, *J. Appl. Phys*. **68**, 2901(1990).
14. R.A.White, and K.A.Dahmen, *Phys*. *Rev.Lett*. **91**. 085702 (2003)

15. C. Cizeau, S. Zapperi, G. Durin, and H. E. Stanley, *Phys*. *Rev. Lett*. **79**, 4669 (1997)
16. Shuqiang Yang, and J.L. Erskine , *Phys*, *Rev*. B **72**, 064433 (2005)
17. Ezio Puppin and Simona Ricci, *Applied Phys*, **76**,17 (2000)
18. K. An, X. Ma, C. Pai, J. Yang, K.Olsson, J.L.Erskine, D.C. Ralph, R.A. Buhrman, and X. Li, *Phys. Rev*. B (R), **93**, 140404, (2016)
19. Richard M. Bozorth, *Ferromagnetism* , Van Nostrand, New York (1953)
20. K. An, J. Yang, (unpublished).